# Design and Implementation of a Reconfigurable Phase Shift Full-Bridge Converter for Wide Voltage Range EV Charging Application

Lyu, Dingsihao ; Soeiro, Thiago Batista; Bauer, Pavol

**DOI**
10.1109/TTE.2022.3176826

**Publication date**
2023

**Document Version**
Final published version

**Published in**
IEEE Transactions on Transportation Electrification

# Design and Implementation of a Reconfigurable Phase Shift Full-Bridge Converter for Wide Voltage Range EV Charging Application

Dingsihao Lyu, *Graduate Student Member, IEEE*, Thiago Batista Soeiro, *Senior Member, IEEE*, and Pavol Bauer, *Senior Member, IEEE*

***Abstract*— This article analyzes, designs, and tests a reconfigurable phase shift full-bridge (r-PSFB) isolated dc/dc converter well suited for a wide voltage operating range. By controlling the auxiliary switches, a series or parallel connection can be realized on the secondary side of the converter. As a result, the r-PSFB converter can operate in an extremely wide voltage range without compromising the system efficiency. In this article, the characteristics of the r-PSFB converter and its design considerations are discussed in detail. An 11-kW r-PSFB converter prototype with 640–840-V input voltage and 250–1000-V output voltage ranges is developed and tested to validate the analysis and efficiency of the designed converter. A comparative study against a conventional PSFB converter is conducted for benchmark purposes to prove the advantages of the studied r-PSFB converter.**

***Index Terms*— Battery charging, electric vehicle (EV) charging, isolated dc/dc converter, reconfiguration, versatile converter, wide voltage range.**

## I. Introduction

THE electric vehicle (EV) market has been expanding with an unprecedented speed in the last decade. The EV cars stock market nearly doubled from 2018 to 2020, as shown in [1]. Along with this trend, the demand for public EV charging stations rises. While the most common EV battery voltage architecture is 400 V, adopted by many manufacturers, namely, Tesla, Nissan, and so on, new high-end EV models with 800-V battery voltage architectures are introduced to the market. Examples are Porsche Taycan [2], Hyundai IONIQ 5 [3], Rapide E from Aston Martin [4], and Lucid Air from Lucid Motors [5]. Therefore, the challenge for the EV chargers is clear: to provide charging services to different cars, which will demand the power electronic circuits to operate with extremely wide battery voltage ranges.

Manuscript received 3 January 2022; revised 23 March 2022; accepted 15 May 2022. Date of publication 20 May 2022; date of current version 21 February 2023. This work was supported in part by the European H2020 Research and Innovation Program, in part by the ECSEL Joint Undertaking, and in part by the National Funding Authorities from eight participating countries, such as Austria, Finland, Germany, including the Free States of Saxony and Thuringia, Hungary, The Netherlands, Slovakia, Spain, and Switzerland, under Grant 826417. *(Corresponding author: Dingsihao Lyu.)*

Dingsihao Lyu and Pavol Bauer are with the Faculty of Electrical Engineering, Mathematics and Computer Science (EEMCS), Delft University of Technology (TU Delft), 2628 CD Delft, The Netherlands (e-mail: d.lyu@tudelft.nl; p.bauer@tudelft.nl).

Thiago Batista Soeiro is with the European Space Research and Technology Centre (ESTEC), European Space Agency (ESA), 2200 AG Noordwijk, The Netherlands (e-mail: thiago.batistasoeiro@esa.int).

Digital Object Identifier 10.1109/TTE.2022.3176826

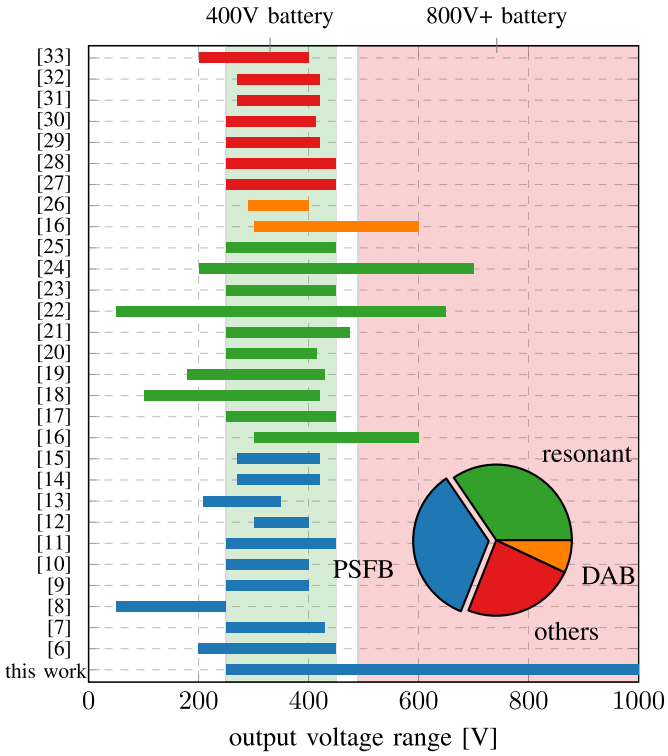


Fig. 1. Output voltage ranges of the dc/dc converter prototypes reported in the literature over the last decade (only the studies with prototype design and testing are included).

However, to the best of our knowledge, there is no study in the literature that has provided experimentally verified isolated dc/dc converters for battery charging that is able to charge both the 400- and 800-V EVs [6]–[33]. Fig. 1 shows the output voltage ranges of the available literature of dc/dc converters researched for the EV charging application from the year of 2011 up to 2021. It is shown that, while most of the designs are focused on the 400-V EV charging, none can charge both the 400- and 800-V EVs.

The problem lies in the poor efficiency performance when these converters are made to operate in such a wide voltage range. As can be seen from Fig. 1, the most popular isolated dc/dc converter topologies used in EV charging are the phase shift full-bridge (PSFB) converter and the series resonant circuits.

PSFB converters are widely used in EV charging application [6]–[15]. For the PSFB type converter, the highest efficiency is obtained at the smallest phase shift or, in other words, the highest operating output voltage. The efficiency will drop as the phase shift increases or the output voltage decreases. The work developed [7] proposes a hybrid-switching PSFB converter that provides a wide ZVS range for the leading leg and ZCS for the lagging leg. Interestingly, the freewheeling circulating losses can also be avoided, and the undesirable voltage overshoots can be clamped well. However, additional passive components (two diodes, a capacitor, and an inductor) are needed, and the complexity of the converter increases. The work in [8] proposes a secondary-side PSFB converter that extends the soft-switching operation and eliminates the circulating current, but it comes with the cost of two additional switches and more complex control. In [13], a ZVS full-bridge dc/dc converter is proposed, which incorporates a diode clamping circuitry on the primary side for the voltage ringing clamping and uses an asymmetrical PWM modulation together with an additional auxiliary inductor to reduce circulating losses.

Due to its simple structure and ability of soft-switching, resonant converters are also widely used for EV charging [16]–[25]. The resonant converter is typically controlled by frequency modulation. The highest efficiency is typically achieved when the switching frequency is close to the resonant frequency in the inductive region of the resonant tank, i.e., when the converter voltage gain is mostly given by the transformer turns ratio, and the H-bridge inverter operates with zero-voltage-switching (ZVS) turn-on. The efficiency of the resonant converter will drop when the voltage regulation is necessary, particularly at low voltage values where the circuit has to operate deeply in the inductive equivalent impedance of the resonant tank. In order to improve the ZVS performance and efficiency of the resonant converter in the wide output voltage range EV charging application, the work in [18] proposes to connect the $LLC$ converter to a SEPIC converter. The SEPIC converter can follow the EV battery voltage and provide a wide dc-link voltage range so that the $LLC$ converter can always operate in proximity of the resonant frequency. The work in [19] proposes to reduce the switching frequency range of the $LLC$ converter by adding delay-time control on the secondary side rectifier switches, which unavoidably increases the cost and complexity of the converter. Lee *et al.* [22] suggest the addition of a buck converter to the $LLC$ converter so that the $LLC$ converter operates with a fixed switching frequency, and the buck converter is responsible for the voltage regulation. However, the buck converter still suffers from an efficiency drop when operated at a low duty cycle. In [24], a three-level $CLLC$ resonant converter is presented, whereby, combining the working modes of the three-level full-bridges, the voltage regulation range is extended, while the controllable switching frequency is kept within a reasonable range. The work in [25] introduces an asymmetric parameters methodology for designing the $CLLC$ converter for EV charging application so that the switching frequency range can be reduced for the bi-direction EV charging application.

Unfortunately, none of these studies have investigated the charging of 800-V EVs, and no experimental results have shown high-efficiency performance in the operation range of 400- and 800-V EV chargings, which is crucial for the current and future EV charging applications. Moreover, when the charging voltage up to 1000 V has to be considered, the usage of rectifier diodes with 1700-V voltage rating becomes necessary if the aforementioned topologies are used, which are more commercially limited and less compatible compared to 650- and 1200-V ones, which have a broad application range in several other markets.

In order to extend the output voltage conversion range of a PSFB converter without compromising the system efficiency performance in the whole operational range, Sun *et al.* [34] proposed the idea of a reconfigurable structure PSFB converter, which can be reconfigurable by connecting its two isolated outputs in series for the high-voltage operation and parallel for the high-current operation. This idea is further extended in [35]–[38], where a wide input voltage range of 100–400 V and the output voltage range of 15–96 V are realized with more reconfigurable steps on the secondary side and one more switching leg on the primary side to enable the series and parallel reconfigurations in the primary side. Since this idea of the reconfigurable structure also enables the utilization of lower current and voltage rating devices on the secondary sides and does not bring extra complexity to the control stage, it seems well suited for the wide output voltage EV charging application. The paper from Sun *et al.* [34] focuses on the design of a constant peak power protection control scheme for the circuit, a nonlinear smooth transition control method for the two configurations, and the stability analysis of the reconfigurable structure. The works presented in [35]–[38] describe more in detail the circuit operation principle and design considerations, including the separate transformer design for better thermal management, ZVS performance, and loss calculation for the reconfigurable PSFB (r-PSFB) converter. However, the steady-state analytical model for calculating the current stresses of the circuit's components, which requires adjustments to that of the conventional PSFB converter, is not elaborated. The voltage ringing issue on the secondary side, which is inherent for the PSFB type converter, is not addressed in these works, whereas, in the EV charging application, where the output voltage is up to 1000 V, the voltage ringing needs to be well-clamped to ensure the safe operation of the rectifier diodes. Moreover, the aforementioned works have not considered different output filter structures, which requires different numbers and voltage/current ratings of the filter components. This tradeoff has to be examined in the EV charging application. Last but not least, no actual benchmark comparison between the r-PSFB converter and the conventional PSFB converter has been carried out for the wide voltage range necessary for the EV charging application.

This article designs and implements an r-PSFB converter based on the idea of the wide output range and constant peak power (RS-WOCP) converter from Sun *et al.* [34] for the wide output voltage EV charging application. Compared to a traditional PSFB converter, the operational phase shift

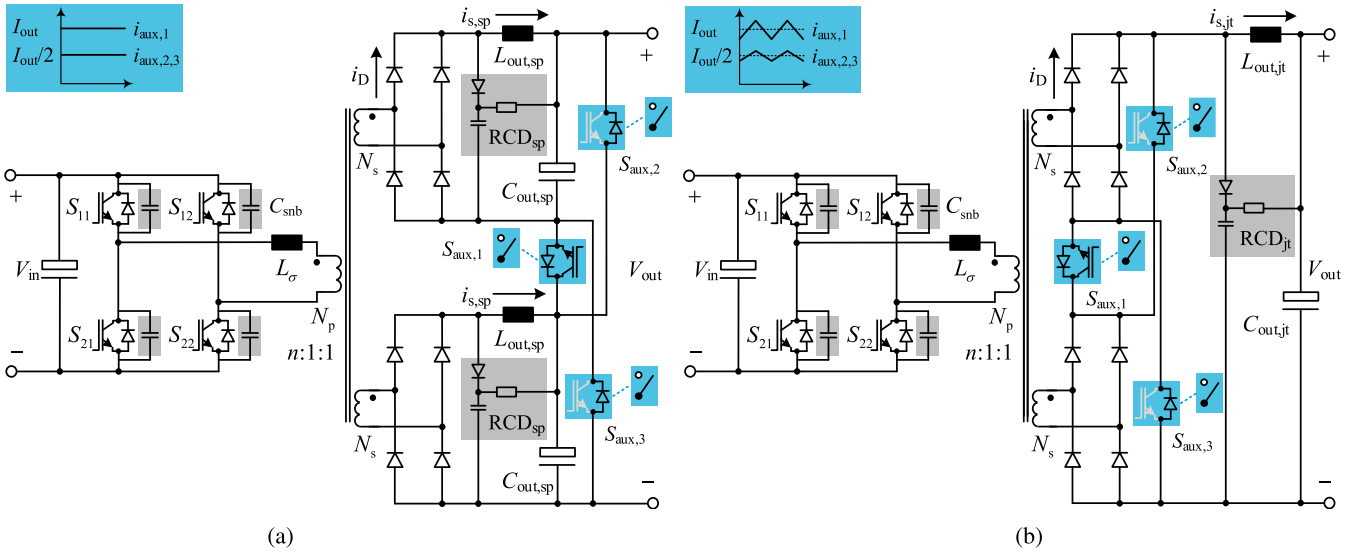


Fig. 2. r-PSFB converter with separate or joint output filter and RCD snubber with $i_{aux,1,2,3}$ illustrated. Note that $S_{aux,1,2,3}$ can be either mechanical switches or semiconductor transistors. The separate output filter structure is chosen in this work for further analysis and design. (a) Separate output filter and RCD snubber (selected topology). (b) Joint output filter and RCD snubber.

angle of the converter during the charging of the low voltage battery is reduced, resulting in high efficiency in a larger operational output voltage range. In the series connection mode, the output voltage of the converter is twice that of a single secondary side, allowing the converter to charge up to 1000 V without the necessity of employing higher voltage rating devices (e.g., 1700-V Schottky diodes), while, in the parallel connection mode, the converter can charge the 400-V EVs more efficiently due to the reduced current stresses on the components. Another important point to highlight is that most of the conventional EVs designed for the lower cost mass market will employ the conventional 400-V battery. Therefore, an EV charger may be mostly used for this voltage class. Based on this, it is wise to implement circuits where high power efficiency is found within the 400-V battery charging profile, even if the output voltage range covers the 800-V battery charging. Unfortunately, the conventional PSFB and most resonant converters used for EV charging would feature a buck-type regulation, and naturally, the peak efficiency range would be found at the highest voltage range, i.e., the 800-V EV battery class. This technical feature highlights the suitability of the r-PSFB converter for the application of EV charging.

The contribution of this article is given as follows.

1) Extended analysis and comparison of the two possible output filter and snubber circuitry structures of the r-PSFB converter.
2) The detailed steady-state model of the r-PSFB converter is presented and verified, while the modification to the conventional PSFB converter is explained thoroughly.
3) The complete design guideline of the r-PSFB converter is elaborated, including the essential snubber circuitry design.
4) The benchmark design of an 11-kW r-PSFB converter and a conventional PSFB converter for the wide output voltage range (250–1000 V) EV charging application is presented, which was not yet elaborated on in the literature. This is particularly important because it identifies the r-PSFB converter as an outstanding solution for the future EV market.
5) The experimental results show excellent charging cycle efficiency for both 400- and 800-V EV battery chargings and a peak efficiency of 98.3% using SiC switches, which is among the highest reported in the available literature analyzing the PSFB converter in the EV charging application with proven prototype experimental results.

This article is arranged as follows. In Section II, the structure, the reconfiguration by the auxiliary switches, and the operation principle of the r-PSFB are introduced. In Section III, the steady-state analytical modeling of the r-PSFB converter is presented. In Section IV, the design requirements based on the existing charging standards are introduced. In Section V, an 11-kW r-PSFB converter and a conventional PSFB converter are designed with the same requirements for the wide voltage range EV charging application. Finally, the experimental test of the r-PSFB prototype is presented in Section VI, in which the efficiency performance of the r-PSFB converter prototype over the whole operational range is shown. An IGBT and an SiC MOSFET are chosen for the benchmark of efficiency performance. The comparison between the r-PSFB and conventional PSFB converter is also explained in Section VI. The conclusion of the work is presented in Section VII.

## II. Operating Principle of the r-PSFB Converter

### A. Schematics

There are two possible structures that can be implemented for the r-PSFB converter, namely, the separate output filter structure and the joint output filter structure. Fig. 2 shows the circuit schematics of these two possible r-PSFB converters.

Three-winding transformer is used, which has one primary and two secondary windings, with the turns ratio $n$:1:1. The primary side is fed by the dc input voltage $V_{\text{in}}$ and a full-bridge inverter. An equivalent leakage inductance $L_\sigma$ is present in the primary side, which is utilized for the ZVS turn-on of the transistors. Each of the secondary sides is connected to a diode bridge rectifier. For the separate output filter structure, as shown in Fig. 2(a), each diode-bridge rectifier is connected to an output filter, $L_{\text{out}}$ and $C_{\text{out}}$, and an RCD snubber circuitry. Three auxiliary switches, $S_{\text{aux,1,2,3}}$, connect the two secondary sides and enable two different configurations according to their switching states. For the joint output filter structure, as shown in Fig. 2(b), the two diode-bridge rectifiers are first connected to $S_{\text{aux,1,2,3}}$, and they share a common output filter and RCD snubber. The RCD snubber circuitry is used for mitigating the voltage spikes on the secondary side diodes [39]. The lossless turn-off snubber $C_{\text{snb}}$ for the H-bridge is also shown on the primary side of the transformer. The auxiliary switches can be implemented by either mechanical switches or semiconductor transistors, as shown in Fig. 2.

### *B. Reconfiguration by the Auxiliary Switches*

In an EV charging session, before the actual energy transfer happens, there is a communication period. During this period, the EV will inform the charger about the required charging voltage and current value [40]. By comparing the voltage value to a preset boundary voltage value $V_{\text{re}}$, the r-PSFB converter can be configured into a parallel connection configuration if the required charging voltage value is lower or as a series connection if the value is higher, by setting the states of the auxiliary switches $S_{\text{aux,1,2,3}}$. It is important to mention that the r-PSFB converter does not need to change the configuration during operation in the EV charging application. This is because the voltage range of the 400-V EVs does not overlap with the 800-V EVs [41]. Therefore, the boundary voltage value $V_{\text{re}}$ can be set to be higher than the maximum charging voltage of the 400-V EV batteries and lower than the minimum charging voltage of the 800-V ones, such as 500 V. As a result, the converter operates only in series connection when charging 400-V EVs and operates only in parallel connection when charging 800-V EVs. With this mechanism, the use of mechanical switches as the auxiliary switches for the reconfiguration, such as relays, is possible, which has less cost and lower equivalent conduction resistance. The detailed explanation is given as follows.

*1) Series Connection:* When $S_{\text{aux,1}}$ is kept ON, while $S_{\text{aux,2,3}}$ are maintained OFF, the negative rail of the upper rectifier is connected with the positive rail of the lower rectifier, making the two secondary side circuits connected in series. This configuration, in principle, enables the converter to supply high output voltage with the utilization of diodes and capacitors with halved voltage rating compared to those of the conventional approach.

*2) Parallel Connection:* When $S_{\text{aux,1}}$ is kept OFF, while $S_{\text{aux,2,3}}$ are maintained ON, the positive and negative rails of the two rectifiers are connected in parallel. The parallel connection configuration enables the converter to operate in the low output voltage range with lower current stresses on the components.

TABLE I

COMPARISON OF THE CURRENT AND VOLTAGE STRESSES BETWEEN FIG. 2(a) AND (b)

| | **separate structure** | **joint structure** |
|---|---|---|
| $V_{\text{stress}}$ of $D_{\text{RCD}}$ | $V_{\text{cp}}$ | $2V_{\text{cp}}$ |
| $V_{\text{stress}}$ of $C_{\text{RCD}}$ | $V_{\text{cp}}$ | $2V_{\text{cp}}$ |
| $V_{\text{stress}}$ of $C_{\text{out}}$ | $V_{\text{out}}/2$ | $V_{\text{out}}$ |
| $V_{\text{stress}}$ of $S_{\text{aux,1}}$ | $V_{\text{out}}$ | $2V_{\text{cp}}$ |
| $V_{\text{stress}}$ of $S_{\text{aux,2,3}}$ | $V_{\text{out}}/2$ | $V_{\text{cp}}$ |
| $I_{\text{stress}}$ of $S_{\text{aux,1}}$ | $I_{\text{out}}$ | $i_{\text{s,jt}}$ |
| $I_{\text{stress}}$ of $S_{\text{aux,2,3}}$ | $I_{\text{out}}/2$ | $i_{\text{s,jt}}/2$ |

### *C. Comparison Between the Two Structures of the r-PSFB Converter*

While the primary side H-bridge, transformer, and secondary side rectifier diode bridges are identical, the two different structures shown in Fig. 2 have differences regarding the output $LC$ filter, the RCD clamping snubber circuitry, and the auxiliary switches.

From the perspective of the component counts, the separate output filter structure has double component counts for the RCD snubber circuitry and the $LC$ filter.

However, the separate output filter structure enables the usage of low-voltage-rating diodes and capacitors for $D_{\text{RCD}}$, $C_{\text{RCD}}$, and $C_{\text{out}}$, whose voltage rating is half compared to that of the joint output filter structure. This is particularly interesting in the EV charging application where the voltage is up to 1000 V, as it enables the usage of 1200 V or even lower voltage rating diodes for the RCD circuitry, which is much more commercially available and compatible compared to the 1700-V diodes that have to be used in the joint output filter structure. From the perspective of cost, components with lower voltage ratings usually have lower costs. Thus, the usage of halved voltage rating components' counters the double components' count.

In addition, the separate output filter structure has slightly lower current and voltage stress on $S_{\text{aux,1,2,3}}$. Placing before $L_{\text{out}}$, $S_{\text{aux,1,2,3}}$ in the joint structure needs to block the rectifier diode bridge voltage, and the current passing through has the current ripple that is determined by $L_{\text{out}}$. In comparison, in the separate structure, $S_{\text{aux,1,2,3}}$ needs to block the output voltage, and the current through $S_{\text{aux,1,2,3}}$ in the separate structure equals the average of that of the joint structure but without the current ripple. As a result, the separate structure enables the usage of slightly lower current/voltage rating switches for $S_{\text{aux,1,2,3}}$ or has less conduction loss compared to the joint structure when the same switches are used. The comparison of the current and voltage stresses between the separate and joint structure is summarized in Table I. $V_{\text{cp}}$ represents the clamping voltage determined by the RCD clamping snubber circuitry, which will be further explained in Section V.

Moreover, the separate output filter structure has a better performance clamping the diode voltage on the two secondary sides because the two separate output capacitors help share the output current evenly on the two secondary sides. On the other hand, in the joint filter structure, the diode voltage on

TABLE II
CIRCUIT PARAMETERS IN THE EQUIVALENT PSFB SHOWN IN FIG. 3

| | series connection | parallel connection |
|---|---|---|
| $S_{\text{aux,1,2,3}}$ | 1,0,0 | 0,1,1 |
| $n_{\text{eff}}$ | $n/2$ | $n$ |
| $L_{\text{out(eff)}}$ | $2L_{\text{out,sp}}$ | $L_{\text{out,sp}}/2$ |
| $C_{\text{out(eff)}}$ | $C_{\text{out,sp}}/2$ | $2C_{\text{out,sp}}$ |
| $i_{\text{Ws(eff)}}$ | $i_{\text{Ws}}$ | $2i_{\text{Ws}}$ |
| $i_{\text{D(eff)}}$ | $i_{\text{D}}$ | $2i_{\text{D}}$ |
| $i_{\text{s(eff)}}$ | $i_{\text{s,sp}}$ | $2i_{\text{s,sp}}$ |

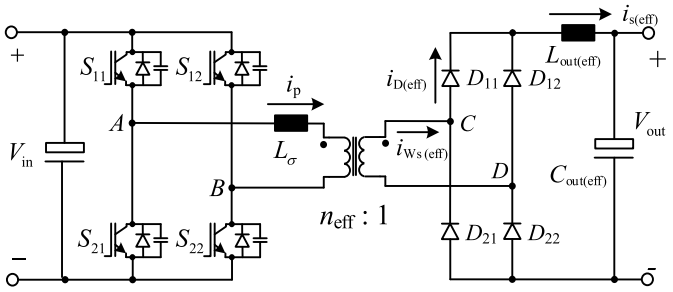


Fig. 3. Equivalent circuit of Fig. 2(a) without the RCD snubber circuits.

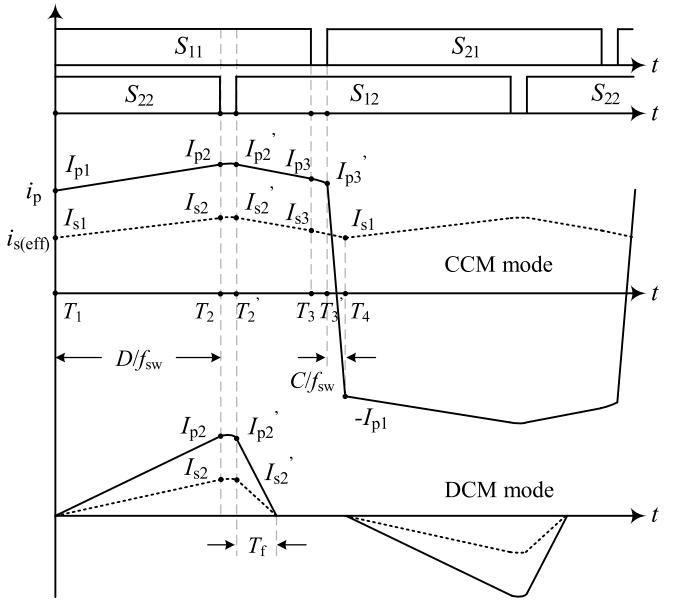


Fig. 4. Typical switching signals and current waveform of the PSFB converter in CCM and DCM.

the two secondary sides is prone to uneven sharing due to the mismatch of the diode resistance between the two sides. As a result, the joint output filter structure has a higher risk of overvoltage on the diodes.

Last but not least, the separate output filter structure facilitates thermal distribution, as the losses are divided into two parts instead of concentrating on one spot.

In conclusion, in the EV charging application, the halved voltage stress, less current stress, better voltage clamping, and thermal distribution of the separate structure shown in Fig. 2(a) prevail over the higher component counts compared to the joint structure shown in Fig. 2(b). The joint structure can be a better candidate in the low-power/-voltage application, where the usage of the common 650-/1200-V diodes is possible, and the inductor does not have a severe thermal issue. The r-PSFB converter with the separate output filter and RCD snubber will be further analyzed and designed in this work.

### D. Operating Principle

Being either the series or parallel connection configuration, the r-PSFB converter shown in Fig. 2(a) can be seen as equivalent to a conventional PSFB with a turns ratio of $n_{\text{eff}}$:1, an output inductor $L_{\text{out(eff)}}$, and an output capacitor $C_{\text{out(eff)}}$, whose values change for the two configurations. Fig. 3 shows the schematics of the equivalent conventional PSFB converter of the r-PSFB converter, and Table II lists the equivalent circuit parameters for the series and parallel configurations.

Like the conventional PSFB converter, the r-PSFB converter is typically controlled with a fixed switching frequency by phase shift modulation where the two half-bridge legs are operated with a 50% duty cycle. The phase shift refers to the asynchronization between the operation of the two half-bridge legs. When the phase shift is null, the diagonal pair of transistors ($S_{11}$ & $S_{22}$, or $S_{12}$ & $S_{21}$) turn on and off synchronously, making the primary side voltage $v_{\text{AB}}$ alternate between $+V_{\text{in}}$ and $-V_{\text{in}}$, which is equivalent to a bipolar modulation of the H-bridge inverter. When the phase shift is nonnull, the synchronization is broken, and the parallel pair of transistors ($S_{11}$ & $S_{12}$, $S_{21}$ & $S_{22}$) are able to be kept turned on at the same time, creating a third circuit state that is $v_{\text{AB}} = 0$ V, leading to a controllable unipolar modulation action. Due to the impressed $i_p$ caused by $L_\sigma$ and inverter bridge capacitance, the switching transition in each half-bridge leg creates a lowered $di_p/dt$ and $dv_{\text{AB}}/dt$ on the primary side, making the ZVS turn-on possible and lowering the turn-off losses of the transistors. Fig. 4 shows the typical switching signals and current waveform of the PSFB converter in the continuous conduction mode (CCM) and the discontinuous conduction mode (DCM).

The operation can be divided into five phases: the active phase where the diagonal transistors conduct ($T_1 - T_2$), the reactive phase where the parallel transistors conduct ($T_2' - T_3$), the commutation phase where the secondary side current commutes among the rectifier diodes ($T_3' - T_4$), and two transition phases during the dead time of each bridge ($T_2 - T_2'$ and $T_3 - T_3'$). A complete description of the operation of a PSFB converter can be found in [42]. The r-PSFB converter can be modeled in the same way as an equivalent PSFB converter with the relation shown in Table II.

## III. STEADY-STATE ANALYTICAL MODELING OF THE R-PSFB

The steady-state analytical model of the r-PSFB in CCM and DCM is introduced and verified by simulation in this section. For the simplicity of the circuit analysis, the following assumption is made.

1) $T_2 = T_2'$, $I_{p2} = I_{p2}'$, and $I_{s2} = I_{s2}'$.
2) $T_3 = T_3'$, and $I_{p3} = I_{p3}'$.

TABLE III

CLOSED-FORM STEADY-STATE ANALYTICAL MODEL OF THE CURRENT STRESSES ON THE TRANSISTORS OF THE r-PSFB CONVERTER. HEREIN, IT IS ASSUMED THAT THE BODY DIODES OF THE MOSFETS DO NOT CONDUCT, AND THUS, THE MOSFET CHANNELS PROCESS THE WHOLE IMPRESSED CURRENT

| | | IGBT | MOSFET |
|---|---|---|---|
| CCM | $I_{\text{S(lead),rms}}$ | $\sqrt{((I_{s1}^2+I_{s1}I_{s2}+I_{s2}^2)D+2I_{s1}^2T_{02n}f_{sw})/(6n_{eff}^2)}$ | $\sqrt{(-(I_{s2}+I_{s3})(I_{s2}+I_{s1}-I_{s3})C+I_{s1}^2+I_{s2}I_{s1}+I_{s2}^2)/(6n_{eff}^2)}$ |
| | $I_{\text{S(lead),avg}}$ | $((I_{s1}+I_{s2})D+2I_{s1}T_{02n}f_{sw})/(4n_{eff})$ | $((2C+2D-1)I_{s1}+(C+2D-1)I_{s2}-CI_{s3})/(4n_{eff})$ |
| | $I_{\text{AD(lead),rms}}$ | $\sqrt{((1-D-C)(I_{s1}^2+I_{s2}^2+I_{s1}I_{s2})+2f_{sw}I_{s3}^2T_{p20})/(6n_{eff}^2)}$ | 0 |
| | $I_{\text{AD(lead),avg}}$ | $((1-D-C)(I_{s1}+I_{s2})+2f_{sw}I_{s3}T_{p20})/(4n_{eff})$ | 0 |
| | $I_{\text{S(lagg),rms}}$ | $\sqrt{((2f_{sw}T_{02n}-1C+1)I_{s1}^2-I_{s1}(C-1)I_{s2}-I_{s2}^2(C-1))/(6n_{eff}^2)}$ | $\sqrt{(-(I_{s2}+I_{s3})(I_{s2}+I_{s1}-I_{s3})C+I_{s1}^2+I_{s2}I_{s1}+I_{s2}^2)/(6n_{eff}^2)}$ |
| | $I_{\text{S(lagg),avg}}$ | $((2f_{sw}T_{02n}-C+1)I_{s1}-I_{s2}(C-1))/(4n_{eff})$ | $(-CI_{s2}-CI_{s3}+I_{s1}+I_{s2})/(4n_{eff})$ |
| | $I_{\text{AD(lagg),rms}}$ | $\sqrt{f_{sw}I_{s3}^2T_{p20}/(3n_{eff}^2)}$ | 0 |
| | $I_{\text{AD(lagg),avg}}$ | $f_{sw}I_{s3}T_{p20}/(2n_{eff})$ | 0 |
| DCM | $I_{\text{S(lead),rms}}$ | $\sqrt{I_{s2}^2D/(6n_{eff}^2)}$ | $\sqrt{I_{s2}^2(2f_{sw}T_f+D)/(6n_{eff}^2)}$ |
| | $I_{\text{S(lead),avg}}$ | $I_{s2}D/(4n_{eff})$ | $I_{s2}(-2f_{sw}T_f+D)/(4n_{eff})$ |
| | $I_{\text{AD(lead),rms}}$ | $\sqrt{f_{sw}I_{s2}^2T_f/(3n_{eff}^2)}$ | 0 |
| | $I_{\text{AD(lead),avg}}$ | $f_{sw}I_{s2}T_f/(2n_{eff})$ | 0 |
| | $I_{\text{S(lagg),rms}}$ | $\sqrt{I_{s2}^2(2f_{sw}T_f+D)/(6n_{eff}^2)}$ | $\sqrt{I_{s2}^2(2f_{sw}T_f+D)/(6n_{eff}^2)}$ |
| | $I_{\text{S(lagg),avg}}$ | $I_{s2}(2f_{sw}T_f+D)/(4n_{eff})$ | $I_{s2}(2f_{sw}T_f+D)/(4n_{eff})$ |
| | $I_{\text{AD(lagg),rms}}$ | 0 | 0 |
| | $I_{\text{AD(lagg),avg}}$ | 0 | 0 |

This is because the transition phases are very short (tens or several hundred nanoseconds) compared to the other three phases. The influence of them on the overall current waveform is, therefore, negligible.

First, the initial inductor current $I_{s1}$ can be calculated according to the following equation:

$$I_{s1} = I_{\text{out}} - \frac{V_{\text{out}}(V_{\text{in(ref)}} - V_{\text{out}})}{4f_{\text{sw}}L_{\text{total(ref)}}V_{\text{in(ref)}}} \tag{1}$$

where $V_{\text{in(ref)}}$ and $L_{\text{total(ref)}}$ are the reflected input voltage and the total inductance value seen from the secondary side, respectively, and they are calculated by

$$V_{\text{in(ref)}} = V_{\text{in}}/n_{\text{eff}} \tag{2}$$

$$L_{\text{total(ref)}} = L_{\sigma\text{(ref)}} + L_{\text{out(eff)}} = L_{\sigma}/n_{\text{eff}}^2 + L_{\text{out(eff)}}. \tag{3}$$

If $I_{s1} \geq 0$, the converter operates in CCM; otherwise, it works in DCM. In CCM, the duty cycle $D$ is calculated as in (6), and the commutation cycle $C$ is calculated according to (7). In DCM, the current starts from zero; thus, $I_{s1} = 0$. The duty cycle $D$ in DCM is calculated differently, as in (6).

With $I_{s1}$, $D$, and $C$ calculated, $I_{s2,3}$ and $I_{p1,2,3}$ can be determined based on the voltage-second balance on the inductor. $I_{s2}$ can be calculated by (4) for both CCM and DCM operations

$$I_{s2} = I_{s1} + \frac{D(V_{\text{in(ref)}} - V_{\text{out}})}{2f_{\text{sw}}L_{\text{total(ref)}}}. \tag{4}$$

$I_{s3}$ can be calculated by (5) if the converter operates in CCM. If in DCM, $I_{s3}$ equals zero

$$I_{s3} = I_{s2} - \frac{(1 - D^{\text{CCM}} - C)V_{\text{out}}}{2f_{\text{sw}}L_{\text{total(ref)}}}. \tag{5}$$

Furthermore, the current stresses on the components can be calculated. Table III summarizes the closed-form steady-state analytical model of the current stresses on the transistors for the r-PSFB converter. In Table III, $T_{p20}$ and $T_{02n}$ are the times for $i_p$ to drop from $I_{p3}$ to 0 and from 0 to $I_{p1}$, respectively, and they are calculated by (9). $T_f$ is the time for $i_s$ to drop from $I_{s2}$ to 0, and it is calculated by (10), as (6)–(10), shown at the bottom of the next page.

The effective rms and average current stress on the secondary side diodes $I_{\text{D,rms/avg(eff)}}$ can be calculated by (11)–(13). Depending on the configuration, the actual diode current stress can be calculated from the effective value based on Table II

$$I_{\text{D,rms(eff)}}^{\text{CCM}} = \sqrt{(1-C)(I_{s2}^2 + I_{s1}I_{s2}) + CI_{s3}^2 + I_{s1}^2/6} \tag{11}$$

$$I_{\text{D,rms(eff)}}^{\text{DCM}} = \sqrt{I_{s2}^2(2f_{\text{sw}}T_f + D^{\text{DCM}})/6} \tag{12}$$

$$I_{\text{D,avg(eff)}} = I_{\text{out}}/2. \tag{13}$$

The rms current stress on the primary winding of the transformer, $I_{\text{Wp,rms}}$, can be calculated based on (14) and (15), as shown at the bottom of the next page, in CCM and DCM operations, respectively.

The effective rms current stress on the secondary winding of the transformer, $I_{\text{Ws,rms(eff)}}$, can be calculated using the turns ratio $n_{\text{eff}}$ by (16). Depending on the configuration, the actual secondary winding current can be calculated from the effective value based on the conversion shown in Table II

$$I_{\text{Ws,rms(eff)}} = I_{\text{Wp,rms}} \cdot n_{\text{eff}}. \tag{16}$$

In order to show the accuracy of the analytical model, LTspice simulation of an r-PSFB converter using IGBTs is conducted, and the simulation results of the current stresses on the semiconductors are compared to the analytical modeling results, as shown in Fig. 5. The compared current stresses include the leading and lagging leg transistor rms and average current $I_{\text{S(lead/lag),rms/avg}}$, the leading and lagging leg antiparallel diode rms and average current $I_{\text{AD(lead/lag),rms/avg}}$, and the secondary side rectifier diode rms and average current

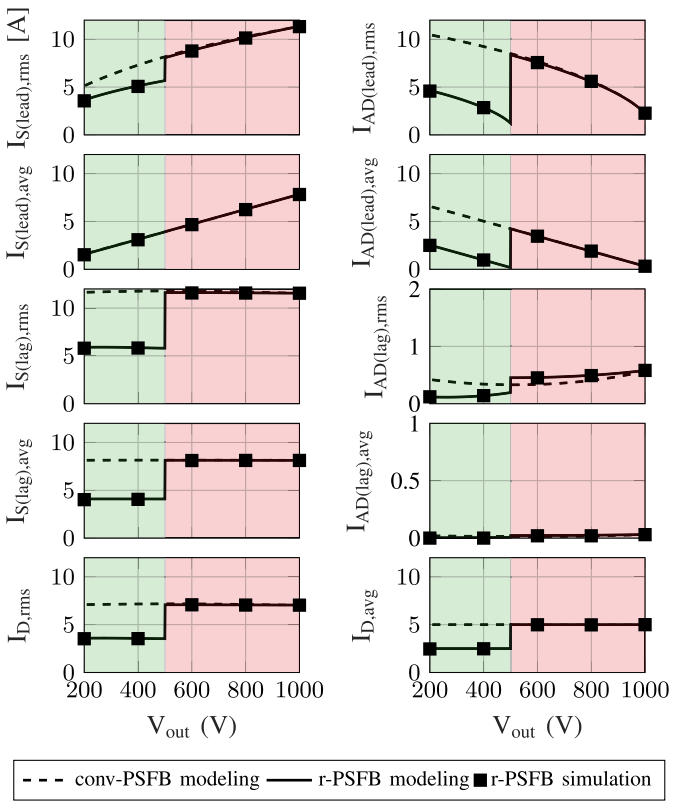


Fig. 5. Analytical modeling and LTspice simulation results of the conventional PSFB and the r-PSFB converter ($V_{in}$ = 640 V, $I_{out}$ = 10 A, and $L_\sigma$ = 10 $\mu$H using IGBT as transistors).

$I_{D,rms/avg}$. It can be seen that the analytical model corresponds well with the simulation model.

## IV. Design Requirements of the Power Module

The design requirements for the r-PSFB converter shown in Fig. 2 are summarized in Table IV.

$V_{out}$ is set to be 250–1000 V, in which the converter operates in the parallel connection mode within 250–500 V and in the series connection mode within 500–1000 V.

TABLE IV
Design Requirements of the r-PSFB Power Module

| requirements | values |
|---|---|
| input voltage $V_{in}$ range | 640-840V |
| output voltage $V_{out}$ range | 250-1000V |
| switching frequency $f_{sw}$ | 15kHz |
| power rating $P$ | 11kW |
| MAX output current $I_{out(max)}$ | 30A |
| MAX output current peak-to-peak ripple $I_{out,ripple(max)}$ | 9A |
| MAX output voltage peak-to-peak ripple $V_{out,ripple(max)}$ | 10V |
| MAX ambient temperature $T_{a(max)}$ | 40°C |

$V_{in}$ is in the range of 640–840 V so that a battery energy storage device, such as a SAMSUNG ESS [43], can be connected to the dc bus between the typically employed grid-connected ac/dc rectifier and this dc/dc converter, allowing power buffering during charging and consequently reducing the grid burden. Therefore, $V_{in}$ is not a controllable parameter, which is different than some designs where the $V_{in}$ could be controlled according to the output voltage [18], [23].

The grid phase voltage in Europe is typically 230 V±10%, which gives a maximum peak line-to-line voltage of 620 V. Considering some nonideal voltage drop on the circuitry and components, the minimum output voltage of the three-phase ac/dc converter is 640 V.

The maximum input voltage is 840 V, which is limited by the input battery, and this enables the usage of the 1200-V voltage rating devices with a 30% safety margin taken into consideration.

The maximum output power is set to be 11 kW to enable the utilization in household applications in the European market. The household three-phase wiring typically has a phase voltage rating of 230 V and a current rating of 16 A. Therefore, the maximum power that can be drawn without modification of the electric wiring is limited to 11 kW.

$I_{out,ripple(max)}$ and $V_{out,ripple(max)}$ are set according to the current version of the charging standards IEC 61851-23:2014 [40].

$$D^{CCM} = \frac{((4I_{out}f_{sw}L_{\sigma(ref)} - V_{out})L_\sigma + V_{in}nL_{out})V_{out}L_{total(ref)}}{-V_{out}(V_{out}L_{\sigma(ref)} + V_{in(ref)}(L_{total(ref)} - L_{\sigma(ref)}))L_\sigma + V_{in}nL_{out}L_{total(ref)}V_{in(ref)}} \tag{6}$$

$$C = \frac{L_{out}L_\sigma(4I_{out}f_{sw}L_{total(ref)} - V_{out})V_{in(ref)} + L_{out}L_\sigma V_{out}^2}{(-L_\sigma(L_{total(ref)} - L_{\sigma(ref)})V_{out} + V_{in}nL_{out}L_{total(ref)})V_{in(ref)} - L_\sigma V_{out}^2 L_{\sigma(ref)}} \tag{7}$$

$$D^{DCM} = 2\sqrt{\frac{I_{out}V_{out}f_{sw}L_{total(ref)}}{V_{in(ref)}(V_{out} - V_{in(ref)})}} \tag{8}$$

$$T_{p20,02n} = I_{p3,p1} \cdot L_\sigma / V_{in} \tag{9}$$

$$T_f = I_{s2} \cdot L_{total(ref)} / V_{out} \tag{10}$$

$$I_{Wp,rms}^{CCM} = \sqrt{\frac{-(I_{s2} + I_{s3})(I_{s2} + I_{s1} - I_{s3})C + I_{s1}^2 + I_{s2}I_{s1} + I_{s2}^2}{3n_{eff}^2}} \tag{14}$$

$$I_{Wp,rms}^{DCM} = \sqrt{\frac{I_{s2}^2(2f_{sw}T_f + D^{DCM})}{3n_{eff}^2}} \tag{15}$$

## V. Design of the 11-kW r-PSFB Converter

### A. Boundary Voltage Value of Reconfiguration $V_{re}$ and the Auxiliary Switches

As it has been explained in Section II-B, the boundary voltage value of reconfiguration $V_{\rm re}$ is the voltage value below which the r-PSFB will be configured into a parallel connection configuration and above which it will be configured as the series connection configuration.

Since the voltage range of the 400-V battery architecture is between 200 and 500 V, and that of the 800-V+ architecture is within the range from 500 to 1000 V, $V_{\rm re}$ is set to be 500 V so that the converter can charge the 400-V EVs in parallel connection configuration and charge the 800-V ones in the series connection configuration.

### B. Transformer Turns Ratio n

The turns ratio can be determined based on the input and output voltage ranges and $V_{\rm re}$. In order to be able to provide a maximum 500-V output voltage in the parallel connection configuration based on $V_{\rm re}$, the transformer turns ratio considering 5% nonideal voltage and duty cycle loss on the components can be calculated as

$$n = \frac{V_{\rm in(min)}}{V_{\rm re}} \cdot 95\% = 1.216. \tag{17}$$

This turns ratio can also ensure a maximum 1000-V output voltage for the series connection configuration.

### C. Output Inductance Value $L_{out}$

Based on the maximum current ripple requirement, the minimum output inductance value $L_{\rm out(min)}$ could be set. The output current ripple in CCM, in which the current of the inductor is always above zero, can be calculated by

$$I_{\rm out,ripple} = \frac{V_{\rm in,ref}(1-D)D}{L_{\rm out}} \cdot \frac{1}{2f_{\rm sw}}. \tag{18}$$

$I_{\rm out,ripple(max)}$ happens when $D = 0.5$ and $V_{\rm in} = V_{\rm in(max)}$. Based on that, $L_{\rm out(min)}$ could be calculated as

$$L_{\rm out(min)} = 2 \cdot \frac{1}{2f_{\rm sw}} \cdot \frac{V_{\rm in(ref,max)}}{4I_{\rm out,ripple(max)}} = 1.3 \text{ mH}. \tag{19}$$

Note that, in the parallel connection mode, the effective inductance value is half of $L_{\rm out}$, as shown in Table II; thus, in order to ensure the maximum current ripple requirement in the parallel connection configuration, the factor 2 in (19) has to be considered.

### D. Output Capacitor $C_{out}$

In the series connection mode of the r-PSFB converter, each of the output capacitor can have a voltage ripple of $0.5V_{\rm out,ripple(max)}$, but, at the same time, the maximum output current ripple can be reached in the series connection mode, which is only $0.5I_{\rm out,ripple(max)}$, when the $L_{\rm out}$ value is designed according to (19). As a result, the minimum capacitance value for the single output capacitor of the r-PSFB converter in the series connection mode operating in CCM can be calculated as

$$C_{\rm out(min)} = \frac{I_{\rm out,ripple(max)}}{16f_{\rm sw}V_{\rm out,ripple(max)}} = 3.75\ \mu\text{F}. \tag{20}$$

When it is in the parallel connection mode, each output capacitor needs to withstand $V_{\rm out,ripple(max)}$, while the current ripple of each output inductor is $0.5I_{\rm out,ripple(max)}$. As a result, in the parallel connection mode, the minimum required output capacitance is halved compared to that of the series connection mode. Overall, the minimum output capacitance value of the r-PSFB converter equals $C_{\rm out(min)}$ calculated in (20).

In the actual experiment, C4AQLBW6130A3NK from KEMET is used for the prototype, which has a capacitance value of 130 $\mu$F and a voltage rating of 500 V. The capacitance value is overrated, but it facilitates the test of the prototype as it provides stable output voltage.

TABLE V

Worst Case Current and Voltage Stresses of the Components for the 11-kW Conv-PSFB and the r-PSFB With the Same Design Requirements, as in Table IV, Assuming That $L_\sigma$ = 10 $\mu$H

| | | conv-PSFB | r-PSFB |
|---|---|---|---|
| worst-case current (A) | $I_{\rm IGBT(lead),rms(max)}$ | 20.8 | 17.7 |
| | $I_{\rm IGBT(lead),avg(max)}$ | 8.8 | 8.7 |
| | $I_{\rm ADIGBT(lead),rms(max)}$ | 31.6 | 18.0 |
| | $I_{\rm ADIGBT(lead),avg(max)}$ | 20.3 | 9.0 |
| | $I_{\rm IGBT(lag),rms(max)}$ | 34.3 | 25.2 |
| | $I_{\rm IGBT(lag),avg(max)}$ | 23.9 | 17.6 |
| | $I_{\rm ADIGBT(lag),rms(max)}$ | 2.8 | 1.7 |
| | $I_{\rm ADIGBT(lag),avg(max)}$ | 0.3 | 0.1 |
| | $I_{\rm D,rms(max)}$ | 21.0 | 15.4 |
| | $I_{\rm D,avg(max)}$ | 15.0 | 11.0 |
| worst-case voltage (V) | $V_{\rm IGBT(max)}$ | 840 | 840 |
| | $V_{\rm D(max)}$ | 1382 | 690 |
| desired V & I ratings (30% margin) | IGBT channel | 1200V, 49A | 1200V, 36A |
| | IGBT anti-parallel diode | 1200V, 45A | 1200V, 26A |
| | rectifier diode | 1974V, 30A | 986V, 22A |
| semiconductor choices | IGBT version | IKQ50N120CT2 | IKW40N120CS6 |
| | SiC MOSFET version | C3M0032120D | IMW120R030M1H |
| | rectifier diode | C5D25170H | IDW30G120C5B |

### E. Semiconductor Choices

With the calculation of the transformer turns ratio $n$ and the output inductance $L_{\rm out}$, the worst case current and voltage stresses on the components can be analyzed based on the analytical modeling if the leakage inductance value $L_\sigma$ is defined, and based on which the current and voltage rating of the semiconductor components can be chosen.

Table V summarizes the worst case current and voltage stresses for the semiconductor components assuming that $L_\sigma$ = 10 $\mu$H, which is close to the value obtained in the designed transformer used in the prototype discussed in Section V. The current stresses are obtained from the analytical modeling, and the voltage stresses are based on the maximum input voltage and turns ratio $n$.

It can be seen that, for the same design requirements, the r-PSFB converter experiences less current stresses on the primary side IGBTs (25.2 A) than the conventional PSFB converter (34.3 A), which means that lower current rating

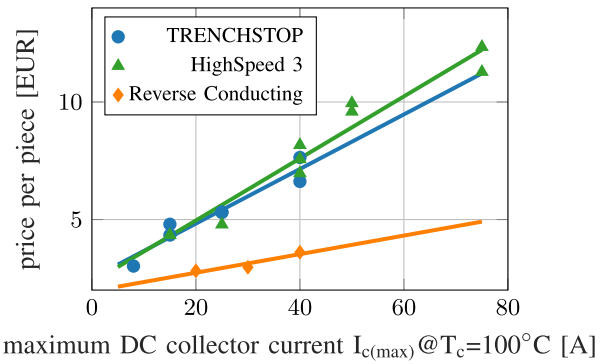


Fig. 6. Cost versus current rating of different Infineon IGBT series. The cost is obtained from Digi-Key per piece on February 2, 2021.

transistors can be utilized in the r-PSFB converter, resulting in lower costs, as indicated in Fig. 6. The primary reason is due to the parallel connection configuration. As can be seen from Fig. 5, all the current stresses except $I_{\mathrm{IGBT(lead),avg}}$ have almost halved current stresses when the circuit is in parallel connection configuration. Note that the maximum power requirement also limits the series connection operation for high output current cases. This is again beneficial for the current stresses as the converter always benefits from the current stress reduction brought by the parallel connection configuration when the output current is high. The same difference is seen in the current stresses of the secondary side rectifier diodes.

Moreover, the voltage stresses on the secondary-side rectifier diodes of the r-PSFB are halved compared to that of the conventional PSFB thanks to the series connection configuration, while the primary side voltage stresses on the transistors are the same. This allows the usage of cheaper and lower voltage rating diodes for the r-PSFB converter.

Considering a 30% safety margin for the current and voltage rating of the IGBT and diode, the ideal current/voltage ratings and the chosen semiconductor components are calculated and listed in Table V. Note that an SiC MOSFET is also selected in order to compare the performance against the IGBT version.

### *F. Magnetic Components' Design*

The procedure for the design of the magnetic components is shown in Fig. 7. In order to avoid an overly large number of solutions, the Litz wire gauge is set to be AWG 41, and the core material for the transformer is Ferrite N87 and for the inductor is Metglas Amorphous Cut Core. Five design variables are considered for finding the optimal design. The core shape for the transformer is the EE core and for the inductor are the UU cores. The number of stacked cores is selected to be within 1–5 for the transformer design and 1–2 for the inductor design. The current density allowed in the wires is set from $4.5 \times 10^6$ to $13.5 \times 10^6$ A/m$^2$. The maximum allowed flux density is set to 80% of $B_{\mathrm{sat}}$ of the core material. The worst case scenarios for the designs of the magnetic components happen when the winding currents are the maximum, which results in the most losses. For the conventional PSFB converter, the worst case scenario is when

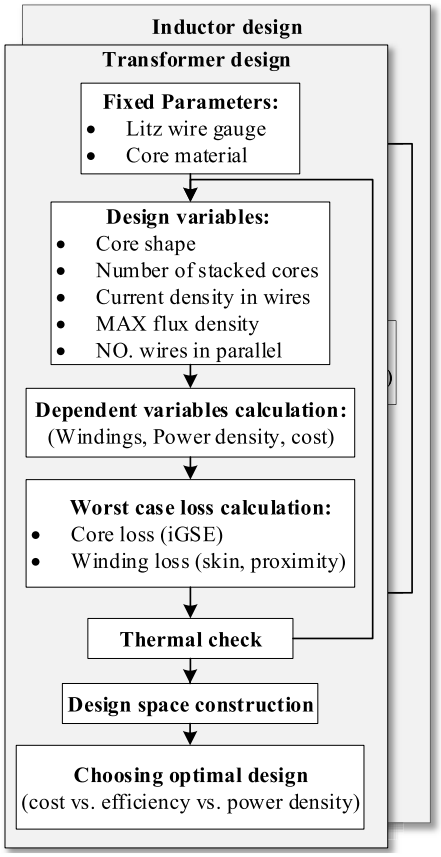


Fig. 7. Design procedure for the magnetic components.

$V_{\mathrm{in}} = 840$ V, $I_{\mathrm{out}} = 30$ A, and $V_{\mathrm{out}} = 366$ V, and for the r-PSFB converter, the worst case scenario is when $V_{\mathrm{in}} = 840$ V, $I_{\mathrm{out}} = 22$ A, and $V_{\mathrm{out}} = 500$ V. The loss calculation is conducted using the method from [44]. Combining the total losses $P_{\mathrm{mag}}$ (W) and the surface area $A_{\mathrm{mag}}$ (m$^2$) of the magnetic components, the temperature rise $\Delta T$ is estimated based on the following equation [45]:

$$\Delta T = \left( \frac{P_{\mathrm{mag}}}{10 \cdot A_{\mathrm{mag}}} \right)^{0.833}. \tag{21}$$

The specifications of the chosen designs are listed in Tables VI and VII, respectively. The winding arrangement indicates the way how the primary and secondary windings are positioned. P-S-S indicates that the primary winding is wounded first and then the two secondary windings on top of it.

There are two interesting observations from Tables VI and VII. First, even though the r-PSFB converter requires the transformer to have two secondary windings and two inductors, compared to the single secondary winding transformer and a single inductor for the conventional PSFB converter, it does not result in increments of total magnetic components losses and core material. This is because the winding current stresses on the magnetic components are more relaxed in the r-PSFB converter compared to its conventional counterpart. Second, it can be seen from Table VII that the temperature rise of the two inductors of the r-PSFB converter

TABLE VI
TRANSFORMER DESIGNS FOR THE CONV-PSFB AND R-PSFB CONVERTERS

| design specs | PSFB | r-PSFB |
|---|---|---|
| switching frequency $f_{sw}$ | 15-kHz | 15-kHz |
| core material | Ferrite N87 | Ferrite N87 |
| core shape | EE 70/33/32 | EE 70/33/32 |
| No. cores stacked | 5 | 5 |
| Litz wire gauge | AWG 41 | AWG 41 |
| Litz wire strands (primary) | 600 | 600 |
| Litz wire strands (secondary) | 600 | 600 |
| No. parallel wires (primary) | 2 | 2 |
| No. parallel wires (secondary) | 1 | 1 |
| No. primary turns $N_{prim}$ | 8 | 12 |
| No. secondary turns $N_{sec}$ | 13 | 10 |
| winding arrangement | P-S | P-S-S |
| MAX flux density $B_{max}$ | 0.186-T | 0.248-T |
| worst-case loss | 66.3-W | 61.5-W |
| temperature rise $\Delta T$ | 54.6°$C$ | 50.2°$C$ |
| power density | 7.2-kW/L | 7.1-kW/L |

TABLE VII
INDUCTOR DESIGNS FOR THE CONV-PSFB AND R-PSFB CONVERTERS

| design specs | PSFB | r-PSFB |
|---|---|---|
| No.inductors | 1 | 2 |
| inductance $L_{out}$ | 1.3-mH | 1.3-mH |
| switching frequency $f_{sw}$ | 15-kHz | 15-kHz |
| core material | Metglas | Metglas |
| core shape | AMCC0080 | AMCC0080 |
| No. cores stacked | 2 | 1 |
| Litz wire gauge | AWG 41 | AWG 41 |
| Litz wire strands | 600 | 600 |
| No. parallel wires | 2 | 2 |
| No. turns $N$ | 34 | 48 |
| MAX flux density $B_{max}$ | 1.248-T | 1.248-T |
| air gap | 1.6-mm | 1.7-mm |
| worst-case loss (single) | 70.2-W | 28.3-W |
| temperature rise $\Delta T$ (single) | 80.0°$C$ | 52.9°$C$ |
| power density (total) | 10.1-kW/L | 7.9-kW/L |

is around 27 °C lower than that of the conventional PSFB converter. This demonstrates that, by having two separate inductors, the thermal management of the r-PSFB converter is simpler than the conventional PSFB converter, as the heat is distributed in two spots.

### *G. Auxiliary Switches*

The auxiliary switches $S_{aux,1,2,3}$ can be implemented by using either semiconductor transistors or mechanical switches. Since the configuration of the r-PSFB converter is determined prior to the charging process, the auxiliary switches do not need to change during the operation of the converter. Therefore, the mechanical switch T9GV1L14-5 is chosen for $S_{aux,1,2,3}$ for the r-PSFB converter prototype, which is a power relay with 30-A current rating. Compared with semiconductor transistors and diodes, the mechanical switches bring fewer conduction losses.

### *H. RCD Snubber Circuitry*

Fig. 8 shows the schematic of the RCD clamping circuitry, with the reflected leakage inductor $L_{\sigma(ref)}$, the transformer

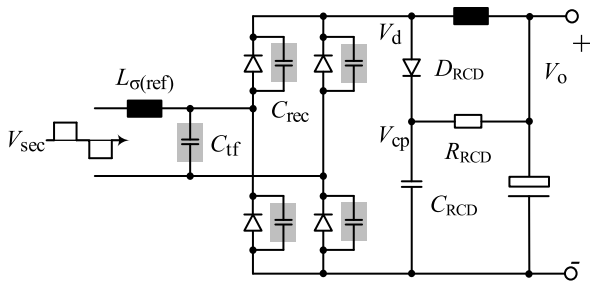


Fig. 8. Schematic of the RCD clamping circuitry.

stray capacitor $C_{tf}$, and the rectifier diode junction capacitor $C_{rec}$ highlighted. Due to the resonance between $L_{\sigma(ref)}$ and the combination of $C_{tf}$ and $C_{rec}$, a voltage ringing will happen on the secondary side diodes with a peak voltage value that can reach twice the value of the secondary winding voltage [39], which can be critical for the safe operation of the rectifier diodes. With the design requirements of this power module stated in Section III, the voltage ringing on the rectifier diodes of the r-PSFB converter, $V_{ringing}$, can be calculated as

$$V_{ringing} = 2 \cdot \frac{V_{in,max}}{n} = 2 \cdot \frac{840}{1.2} = 1400 \text{ V} \tag{22}$$

which will cause overvoltage failure on the 1200-V diodes. Therefore, the RCD clamped snubber circuitry is designed to clamp the voltage ringing to a reasonable value, $V_{cp}$, so that a safe operation for the 1200-V rectifier diodes is ensured.

First, the capacitor of the RCD circuitry, $C_{RCD}$, is chosen to be 200 nF so that it can be regarded as a voltage clamping device with enough energy storage capacity. Second, the clamped voltage value $V_{cp}$ of the r-PSFB converter is set to be 1000 V, considering that 1200-V diodes can be used. The resistance value of the resistor of the RCD circuitry, $R_{RCD}$, can be calculated according to the following equation:

$$R_{RCD} = \frac{(V_{cp} - V_{o(max)}) \cdot (V_{cp} - V_{d(max)})}{f_{sw} \cdot C_{sec} \cdot V_{cp} \cdot (2V_{d(max)} - V_{cp})} \tag{23}$$

in which $V_{o(max)}$ and $V_{d(max)}$ are the maximum output and input voltages of the RCD circuitry, respectively. $C_{sec}$ is the combination of $C_{tf}$ and $C_{rec}$, which can be estimated by measuring the resonant frequency of the voltage ringing, with $L_\sigma$ known. In this r-PSFB converter, $C_{sec}$ is measured to be around 400 pF, $V_{d,max} = 840/1.2 = 700$ V, and $V_{out,max} = 1000/2 = 500$ V. Thus, based on (23), 62-k$\Omega$ resistors are chosen for the RCD snubber. Assuming the same $C_{sec}$, 5.2-k$\Omega$ resistors are chosen for the conventional PSFB converter to clamp the diode voltage at around 1480 V, while diodes with 1700-V voltage ratings are used. The loss dissipated on $R_{RCD}$ can be calculated by

$$P_{RCD} = \frac{(V_{cp} - V_{out,max})^2}{R_{RCD}}. \tag{24}$$

## VI. EXPERIMENTAL RESULTS OF THE R-PSFB PROTOTYPE

Based on the designs in Section IV, an 11-kW, 640–840-V input voltage, 250–1000-V output voltage r-PSFB dc/dc converter prototype is built, and set-point open-loop tests are done

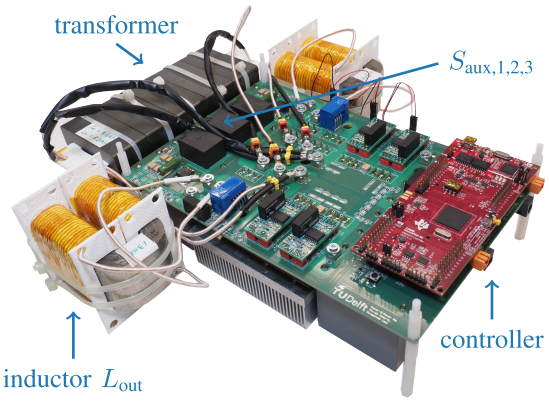


Fig. 9. 11-kW r-PSFB converter prototype.

TABLE VIII
EQUIPMENT USED IN THE EXPERIMENT

| | equipment model |
|---|---|
| microcontroller | TI TMS320F283790 |
| input power supply | Delta Elektronika SM1500-CP-15 |
| output electronic load | Delta Elektronika SM1500-CP-15 |
| power analyzer | Yokogawa WT500 |
| oscilloscope | Yokogawa DLM3000 |

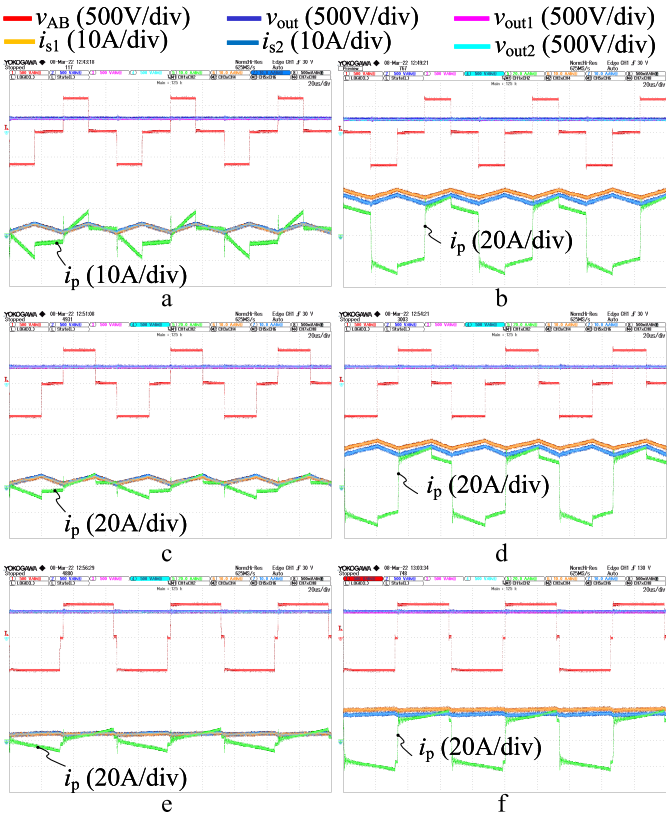


Fig. 10. Operational waveform of the r-PSFB converter in the parallel connection mode with $V_{in} = 640$ V. $v_{out1/2}$ and $i_{s1/2}$ are the output voltage and current of the two secondary side rectifiers, measured after the RCD circuitry and on the output inductors, respectively. (a) $V_{out} = 250$ V, $I_{out} = 5$ A. (b) $V_{out} = 250$ V, $I_{out} = 30$ A. (c) $V_{out} = 320$ V, $I_{out} = 5$ A. (d) $V_{out} = 320$ V, $I_{out} = 30$ A. (e) $V_{out} = 500$ V, $I_{out} = 5$ A. (f) $V_{out} = 500$ V, $I_{out} = 22$ A.

to verify the efficiency performance of the system. Fig. 9 shows the constructed prototype. The power density of the converter is 2.3 kW/L. Table VIII lists the equipment used in the test.

Figs. 10 and 11 show the operational waveform of the r-PSFB converter in parallel and series connection modes under various $V_{out}$ and $I_{out}$ conditions.

From Fig. 10, it can be seen that, in the parallel connection mode, the output current is shared between the two rectifiers, enabling the use of diodes with a lower current rating compared to the conventional PSFB converter. When operating with a 5-A output current, as shown in Fig. 10(a), (c), and (e), the difference in the current of the two secondary sides is unnoticeable. When operating with 30-A output current, as shown in Fig. 10(b), (d), and (f), the current difference becomes observable. This uneven sharing of current is due to the difference in impedance of the two secondary sides, which can come from the transformer's secondary winding, diode resistance and inductor impedance, and relay contact resistance. To have an even current sharing, screening on those components is needed to ensure identical impedance. However, even without screening, less than 2 A of current difference is observed when this r-PSFB prototype is operating with $I_{out(max)}$, which is around 6.7% compared to $I_{out(max)}$. This demonstrates the feasibility of the parallel connection operation of the r-PSFB converter.

From Fig. 11, it can be seen that, in the series connection mode, the output voltage is shared evenly between the two rectifiers, with less than 50-V difference, enabling the use of diodes and capacitors with lower voltage rating compared to the conventional PSFB converter.

Fig. 12 demonstrates the voltage clamping effect of the RCD snubber circuitry with different $V_{in}$ and connection modes. It can be seen that, with the maximum input voltage of 840 V, the diode voltages are clamped exactly at 1000 V in both parallel and series connection modes. Therefore, the safe operation of the 1200-V diodes is ensured.

Fig. 13 shows the tested efficiency of the r-PSFB converter together with the estimated efficiency of the r-PSFB and the conventional PSFB converter. The estimated efficiency is obtained using the steady-state analytical model in Section III, and the loss calculation formulas are introduced in [44] and [46].

It can be seen from Fig. 13 that the tested efficiency of the r-PSFB converter corresponds very well to the estimation. For the IGBT version, the peak efficiency, $\eta_{peak}$, of 97.6% is obtained in series connection mode when $V_{in} = 640$ V, $V_{out} = 1000$ V, and $I_{out} = 10$ A, and an efficiency of 97.4% is tested in the parallel connection mode when $V_{in} = 640$ V, $V_{out} = 490$ V, and $I_{out} = 20$ A. For the SiC MOSFET version, $\eta_{peak}$ of 98.3% is obtained in the series connection mode when $V_{in} = 640$ V, $V_{out} = 1000$ V, and $I_{out} = 10$ A, and 98.2% is tested in the parallel connection mode when $V_{in} = 640$ V, $V_{out} = 490$ V, and $I_{out} = 20$ A.

The benefits brought by the reconfiguration are clearly seen in Fig. 13. First, the r-PSFB prototype has an efficiency jump

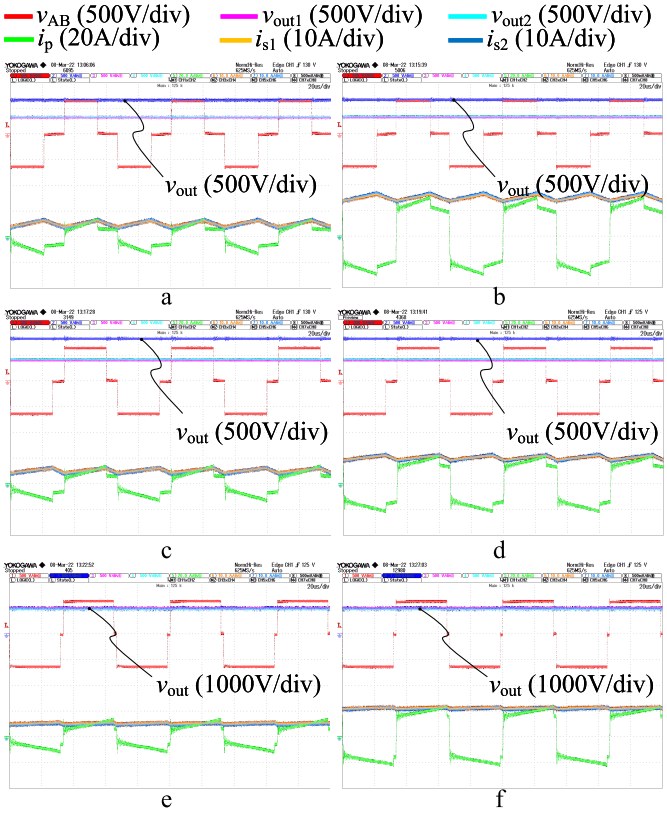


Fig. 11. Operational waveform of the r-PSFB converter in the series connection mode with $V_{in}$ = 640 V. (a) $V_{out}$ = 660 V, $I_{out}$ = 5 A. (b) $V_{out}$ = 660 V, $I_{out}$ = 15 A. (c) $V_{out}$ = 830 V, $I_{out}$ = 5 A. (d) $V_{out}$ = 830 V, $I_{out}$ = 10 A. (e) $V_{out}$ = 1000 V, $I_{out}$ = 5 A. (f) $V_{out}$ = 1000 V, $I_{out}$ = 11 A.

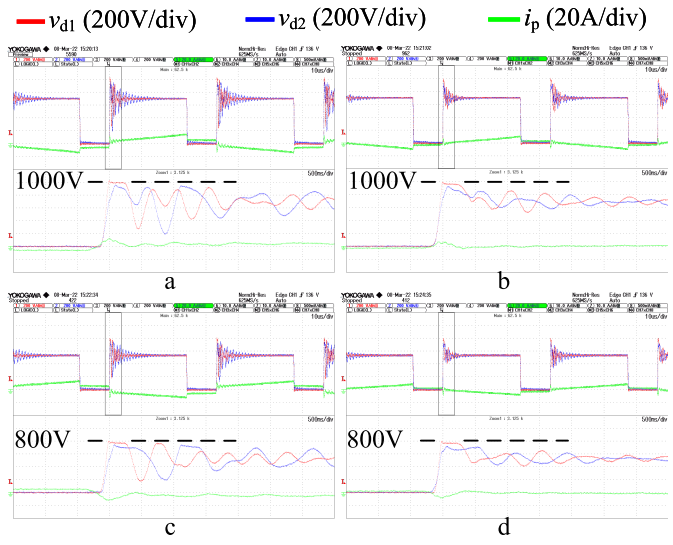


Fig. 12. Voltage clamping of the RCD snubber circuitry. $v_{d1,2}$ is the diode voltage of the two secondary sides. (a) $V_{in}$ = 840 V, series connection. (b) $V_{in}$ = 840 V, parallel connection. (c) $V_{in}$ = 640 V, series connection. (d) $V_{in}$ = 640 V, parallel connection.

when the configuration changes, keeping the efficiency high in a wider voltage range compared to the conventional PSFB. This occurs because the equivalent duty cycle increase leads to lower current stress on the semiconductors, as shown in Fig. 5. From $V_{out}$ = 1000 V, the efficiency of both r-PSFB and

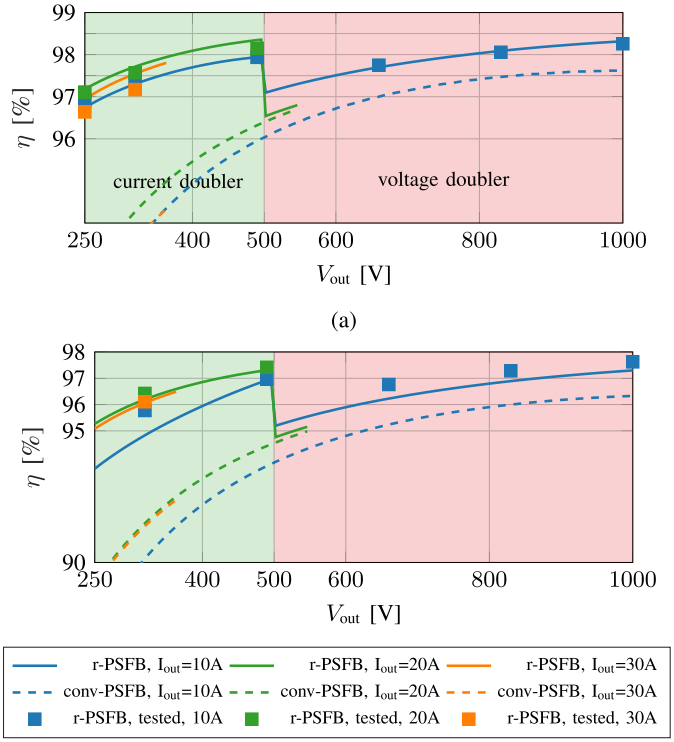


Fig. 13. Estimated and measured efficiencies of the conventional PSFB and the r-PSFB converter ($V_{in}$ = 640 V, $f_{sw}$ = 15 kHz, $L_\sigma$ = 8.6 $\mu$H, $C_{snb}$ = 470 pF, $f_{sw}$ = 15 kHz, $R_g$ = 11 Ω for the IGBT version and 5 Ω for the SiC MOSFET version, and $T_j$ = 125 °C). (a) SiC version. (b) IGBT version.

TABLE IX
ESTIMATED CHARGING CYCLE EFFICIENCY OF THE CONVENTIONAL PSFB AND R-PSFB

| $\eta_{cycle}$ | conv-PSFB (IGBT) | r-PSFB (IGBT) | r-PSFB (SiC) |
|---|---|---|---|
| $\eta_{400V,50.36kWh,CCCV}$ | 92.2 | 96.4 | 97.8 |
| $\eta_{800V,79.2kWh,CCCV}$ | 96.0 | 96.4 | 97.8 |

conventional PSFB converter starts to drop as $V_{out}$ decreases. This is due to the increasing phase shift that is required to step-down $V_{out}$. However, thanks to the reconfiguration from voltage to current doubler, the phase shift of the r-PSFB converter is reset at $V_{out}$ = 500 V. Less current stresses are found on the primary side semiconductors during the current doubler operation ($V_{out}$ = 250 − 500 V), which improves the efficiency performance when $V_{out}$ is low.

For a better comparison between the conventional PSFB and the r-PSFB, the charging cycle efficiency $\eta_{cycle}$ proposed in [46] of the two converters is estimated, which can be calculated by (25). $\eta(t)$ is the instantaneous efficiency of the converter during charging, and $T_c$ is the total charging time

$$\eta_{cycle} = \int_0^{T_c} \eta(t) \cdot dt. \tag{25}$$

Two EV batteries representing a 400-V EV and an 800-V EV are considered: one with 400-V nominal voltage and 50.35-kWh capacity, and the other with 800-V nominal voltage

TABLE X

BENCHMARK OF THE R-PSFB CONVERTER DESIGNED IN THIS WORK WITH THE PSFB TYPE DC/DC CONVERTERS USED FOR EV CHARGING APPLICATIONS FOUND IN THE LITERATURE. $I_{\text{TRANSISTOR}}$ IS THE CURRENT RATING OF THE TRANSISTORS @ $T_c = 100°\text{C}$ USED IN THE LITERATURE; PD IS THE VOLUMETRIC POWER DENSITY

| reference | $V_{\text{out,min}}$ [V] | $V_{\text{out,max}}$ [V] | $I_{\text{out,max}}$ [A] | P [kW] | $\text{type}_{\text{transistor}}$ | $I_{\text{transistor}}$ [A] | $\eta_{\text{peak}}$ [%] | $f_{\text{sw}}$ [kHz] | PD [kW/L] |
|---|---|---|---|---|---|---|---|---|---|
| [6] | 200 | 450 | 11 | 3.3 | Si MOSFET | 29 | 96 | 200 | / |
| [7] | 250 | 420 | / | 3.6 | hybrid | 48 | 98.1 | 42 | / |
| [8] | 50 | 200 | / | 1 | IGBT | 60 | 94 | 50 | / |
| [9], [10] | 250 | 400 | 20 | 6 | SiC MOSFET | 30 | 96.5 | 200 | 12 |
| [11] | 250 | 450 | 4 | 2 | Si MOSFET | 46 | 98.3 | 50 | / |
| [12] | 300 | 400 | / | 1 | / | / | 95 | / | / |
| [13] | 209 | 350 | 3.75 | 1.2 | Si MOSFET | 35 | 95 | 100 | / |
| [14] | 270 | 420 | 7.85 | 3.3 | Si MOSFET | 31.6 | 97.9 | 100 | / |
| [15] | 270 | 420 | 7.85 | 3.3 | Si MOSFET | 31.6 | 98.3 | 50 | / |
| this work | 250 | 1000 | 30 | 11 | IGBT | 40 | 97.6 | 15 | 2.3 |
| this work | 250 | 1000 | 30 | 11 | SiC MOSFET | 45 | 98.3 | 15 | 2.3 |

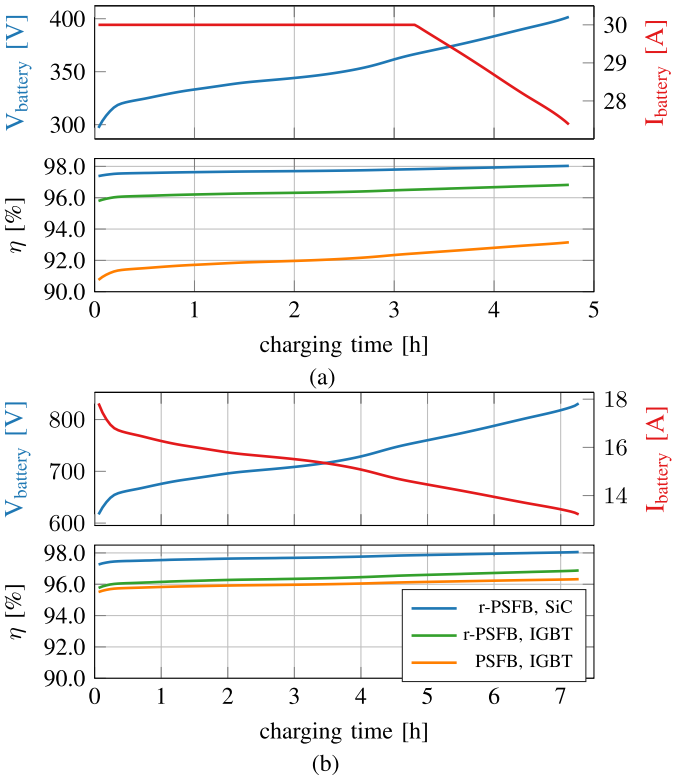


Fig. 14. Charging process of (a) 400-V, 50.35-KWh and (b) 800-V, 79.2-kWh batteries using an 11-kW converter and the efficiency estimation.

and 79.2-kWh capacity. The constant current constant voltage (CCCV) charging profiles of the 11-kW PSFB and r-PSFB converters charging these two EV batteries are simulated using an impedance-based model of a lithium nickel oxide (LNCO) Boston Power SWING 5300 [47]. The charging profiles are shown in Fig. 14. Then, the charging cycle efficiency of charging the 400-V battery, denoted as $\eta_{400\text{ V},50.35\text{ kWh,CCCV}}$, and the 800-V battery, denoted as $\eta_{800\text{ V},79.2\text{ kWh,CCCV}}$, is calculated based on the estimated efficiency. Table IX shows the charging cycle efficiency.

It can be seen that the r-PSFB converter provides the same $\eta_{\text{cycle}}$ for both 400-V and 800-V+ EVs, while the conventional PSFB converter has a significantly poorer $\eta_{\text{cycle}}$ for the charging of 400-V EVs compared to the 800-V EVs. This is mainly due to the large phase shift when $V_{\text{out}}$ is low. On the other hand, as demonstrated, the r-PSFB converter is able to reset the phase shift by changing the series connection mode into the parallel connection mode when charging the 400-V EVs, resulting in less current stress on the semiconductors, which has been observed from Fig. 5. Therefore, the conduction, switching, and magnetic losses are also reduced. Moreover, the loss from the RCD snubber of the conventional PSFB converter is also higher because of the high-voltage difference applied.

Moreover, comparing the IGBT and the SiC versions, even though the $\eta_{\text{peak}}$ of the SiC version is around 0.7% (98.3% − 97.6%) higher than the IGBT version, $\eta_{\text{cycle}}$ is 1.4% (97.8% − 96.4%) higher. This indicates that $\eta_{\text{peak}}$ is the best metric for stating the performance of the converter. During the charging process, the converter operates outside of the $\eta_{\text{peak}}$ point most of the time. As a result, the efficiency performance at the other operational points matters considerably. It can be seen from Fig. 13 that the SiC version has higher efficiency than the IGBT version at the operational area other than the $\eta_{\text{peak}}$ point, which contributes to the difference of $\eta_{\text{cycle}}$.

In addition, the specifications of this r-PSFB prototype are benchmarked against the PSFB type prototypes reported in the IEEE literature in the last decades for EV charging applications, as shown in Table X. It can be seen that this 11-kW prototype covers an unprecedented wide output voltage range from 250 to 1000 V that is able to charge both the 400- and 800-V EVs. Considering the maximum output current and power rating of the prototypes, this work utilizes the most cost-effective semiconductor transistors. $\eta_{\text{peak}}$ of this prototype using cost-effective IGBTs is much higher than the IGBT prototype from [8] but lower than some Si MOSFET prototypes. The SiC version of this prototype reaches the same highest $\eta_{\text{peak}}$ of 98.3% reported in [11] and [15]. This work also provides the charging cycle efficiency $\eta_{\text{cycle}}$, which is considered a better evaluation criterion for the EV charging application.

## VII. CONCLUSION

An r-PSFB converter with an extremely wide voltage range is analyzed, designed, and tested. The converter extends the operational voltage range while keeping high efficiency in the

whole operating range, thanks to the ability of reconfiguration. The operation and design of the converter are explained in detail. Finally, the comprehensive test results of the 11-kW prototype with 640–840-V input voltage and 250–1000-V output voltage are presented, including the calculation of charging cycle efficiency. The results show excellent correspondence between the estimation and test, which, therefore, demonstrates the feasibility of this converter in EV charging applications.

## REFERENCES


[1] IEA. (2021). *Global EV Data Explorer*. [Online]. Available: https://www.iea.org/articles/global-ev-data-explorer

[2] *Porsche Taycan Models*. Accessed: Aug. 23, 2021. [Online]. Available: https://www.porsche.com/international/models/taycan/taycan-models/tayca% n/

[3] *IONIQ 5 Brochure*. Accessed: Aug. 23, 2021. [Online]. Available: https://www.hyundai.co.U.K./brochures/brochure_ioniq5.pdf

[4] (2019). *Production Ready Rapide E Given World Debut at Auto Shanghai*. [Online]. Available: https://www.astonmartin.com/en/our-world/news/2019/04/30/production-ready-rapide-e-given-world-debut-at-auto-shanghai

[5] *Lucid Air*. Accessed: Aug. 23, 2021. [Online]. Available: https://www.lucidmotors.com/air

[6] D. S. Gautam, F. Musavi, M. Edington, W. Eberle, and W. G. Dunford, "An automotive onboard 3.3-kW battery charger for PHEV application," *IEEE Trans. Veh. Technol.*, vol. 61, no. 8, pp. 3466–3474, Jul. 2012, doi: 10.1109/TVT.2012.2210259.

[7] B. Gu, J. Lai, N. Kees, and C. Zheng, "Hybrid-switching full-bridge DC–DC converter with minimal voltage stress of bridge rectifier, reduced circulating losses, and filter requirement for electric vehicle battery chargers," *IEEE Trans. Power Electron.*, vol. 28, no. 3, pp. 1132–1144, Mar. 2013, doi: 10.1109/TPEL.2012.2210565.

[8] T. Mishima, K. Akamatsu, and M. Nakaoka, "A high frequency-link secondary-side phase-shifted full-range soft-switching PWM DC–DC converter with ZCS active rectifier for EV battery chargers," *IEEE Trans. Power Electron.*, vol. 28, no. 12, pp. 5758–5773, Dec. 2013, doi: 10.1109/TPEL.2013.2258040.

[9] B. Whitaker *et al.*, "A high-density, high-efficiency, isolated on-board vehicle battery charger utilizing silicon carbide power devices," *IEEE Trans. Power Electron.*, vol. 29, no. 5, pp. 2606–2617, May 2014, doi: 10.1109/TPEL.2013.2279950.

[10] B. Whitaker, A. Barkley, Z. Cole, B. Passmore, T. McNutt, and A. B. Lostetter, "A high-frequency, high-efficiency silicon carbide based phase-shifted full-bridge converter as a core component for a high-density on-board vehicle battery charging system," in *Proc. IEEE ECCE Asia Downunder*, Jun. 2013, pp. 1233–1239, doi: 10.1109/ECCE-Asia.2013.6579266.

[11] W.-Y. Choi, M.-K. Yang, and H.-S. Cho, "High-frequency-link soft-switching PWM DC–DC converter for EV on-board battery chargers," *IEEE Trans. Power Electron.*, vol. 29, no. 8, pp. 4136–4145, Aug. 2014, doi: 10.1109/TPEL.2013.2288364.

[12] M.-K. Yang, H.-S. Cho, S.-J. Lee, and W.-Y. Choi, "High-efficiency low-cost soft-swtiching DC–DC converter for EV on-board battery chargers," in *Proc. IEEE Appl. Power Electron. Conf. Expo. (APEC)*, Mar. 2015, pp. 2050–2055, doi: 10.1109/APEC.2015.7104631.

[13] V. R. K. Kanamarlapudi, B. Wang, N. K. Kandasamy, and P. L. So, "A new ZVS full-bridge DC–DC converter for battery charging with reduced losses over full-load range," *IEEE Trans. Ind. Appl.*, vol. 54, no. 1, pp. 571–579, Feb. 2018, doi: 10.1109/TIA.2017.2756031.

[14] M.-S. Lee, C.-Y. Lim, K.-W. Kim, M.-H. Park, and G.-W. Moon, "A phase-shift full-bridge converter with novel voltage oscillation clamping circuit for electric vehicle on-board charger," in *Proc. 10th Int. Conf. Power Electron. ECCE Asia (ICPE-ECCE Asia)*, May 2019, pp. 2040–2045, doi: 10.23919/ICPE2019-ECCEAsia42246.2019.8796489.

[15] C.-Y. Lim, Y. Jeong, and G.-W. Moon, "Phase-shifted full-bridge DC–DC converter with high efficiency and high power density using center-tapped clamp circuit for battery charging in electric vehicles," *IEEE Trans. Power Electron.*, vol. 34, no. 11, pp. 10945–10959, Nov. 2019, doi: 10.1109/TPEL.2019.2899960.

[16] Y. Du, S. Lukic, B. Jacobson, and A. Huang, "Review of high power isolated bi-directional DC–DC converters for PHEV/EV DC charging infrastructure," in *Proc. IEEE Energy Convers. Congr. Expo.*, Sep. 2011, pp. 553–560, doi: 10.1109/ECCE.2011.6063818.

[17] J. Deng, S. Li, S. Hu, C. C. Mi, and R. Ma, "Design methodology of LLC resonant converters for electric vehicle battery chargers," *IEEE Trans. Veh. Technol.*, vol. 63, no. 4, pp. 1581–1592, May 2014, doi: 10.1109/TVT.2013.2287379.

[18] C. Shi, H. Wang, S. Dusmez, and A. Khaligh, "A SiC-based high-efficiency isolated onboard PEV charger with ultrawide DC-link voltage range," *IEEE Trans. Ind. Appl.*, vol. 53, no. 1, pp. 501–511, Jan./Feb. 2017, doi: 10.1109/TIA.2016.2605063.

[19] G. Liu, Y. Jang, M. M. Jovanovi, and J. Q. Zhang, "Implementation of a 3.3-kW DC–DC converter for EV on-board charger employing the series-resonant converter with reduced-frequency-range control," *IEEE Trans. Power Electron.*, vol. 32, no. 6, pp. 4168–4184, Jun. 2017, doi: 10.1109/TPEL.2016.2598173.

[20] B.-K. Lee, J.-P. Kim, S.-G. Kim, and J.-Y. Lee, "An isolated/bidirectional PWM resonant converter for V2G(H) EV on-board charger," *IEEE Trans. Veh. Technol.*, vol. 66, no. 9, pp. 7741–7750, Sep. 2017, doi: 10.1109/TVT.2017.2678532.

[21] Z. Li, X. Yang, Y. Li, J. Li, B. Zhang, and T. Lei, "Design and implementation of a high-efficiency DC/DC converter for EVs charging basing on LLC resonant topology and silicon-carbide devices," in *Proc. IEEE Int. Power Electron. Appl. Conf. Expo. (PEAC)*, Nov. 2018, pp. 1–6, doi: 10.1109/PEAC.2018.8590636.

[22] W.-S. Lee, J.-H. Kim, J.-Y. Lee, and I.-O. Lee, "Design of an isolated DC/DC topology with high efficiency of over 97% for EV fast chargers," *IEEE Trans. Veh. Technol.*, vol. 68, no. 12, pp. 11725–11737, Dec. 2019, doi: 10.1109/TVT.2019.2949080.

[23] Z. Zhang, C. Liu, M. Wang, Y. Si, Y. Liu, and Q. Lei, "High-efficiency high-power-density CLLC resonant converter with low-stray-capacitance and well-heat-dissipated planar transformer for EV on-board charger," *IEEE Trans. Power Electron.*, vol. 35, no. 10, pp. 10831–10851, Oct. 2020, doi: 10.1109/TPEL.2020.2980313.

[24] Y. Xuan, X. Yang, W. Chen, T. Liu, and X. Hao, "A novel three-level CLLC resonant DC–DC converter for bidirectional EV charger in DC microgrids," *IEEE Trans. Ind. Electron.*, vol. 68, no. 3, pp. 2334–2344, Mar. 2021, doi: 10.1109/TIE.2020.2972446.

[25] J. Min and M. Ordonez, "Bidirectional resonant CLLC charger for wide battery voltage range: Asymmetric parameters methodology," *IEEE Trans. Power Electron.*, vol. 36, no. 6, pp. 6662–6673, Jun. 2021, doi: 10.1109/TPEL.2020.3033982.

[26] V. M. Iyer, S. Gulur, and S. Bhattacharya, "Optimal design methodology for dual active bridge converter under wide voltage variation," in *Proc. IEEE Transp. Electrific. Conf. Expo (ITEC)*, Jun. 2017, pp. 413–420, doi: 10.1109/ITEC.2017.7993306.

[27] C. Liu *et al.*, "High-efficiency hybrid full-bridge–half-bridge converter with shared ZVS lagging leg and dual outputs in series," *IEEE Trans. Power Electron.*, vol. 28, no. 2, pp. 849–861, Feb. 2013, doi: 10.1109/TPEL.2012.2205019.

[28] I.-O. Lee and G.-W. Moon, "Half-bridge integrated ZVS full-bridge converter with reduced conduction loss for electric vehicle battery chargers," *IEEE Trans. Ind. Electron.*, vol. 61, no. 8, pp. 3978–3988, Aug. 2014, doi: 10.1109/TIE.2013.2282608.

[29] I.-O. Lee, "Hybrid PWM-resonant converter for electric vehicle on-board battery chargers," *IEEE Trans. Power Electron.*, vol. 31, no. 5, pp. 3639–3649, May 2016, doi: 10.1109/TPEL.2015.2456635.

[30] Y.-J. Kim and J.-Y. Lee, "Full-bridge+SRT hybrid DC/DC converter for a 6.6-kW EV on-board charger," *IEEE Trans. Veh. Technol.*, vol. 65, no. 6, pp. 4419–4428, Jun. 2016, doi: 10.1109/TVT.2016.2535237.

[31] C.-Y. Lim, K.-M. Kim, D. Kim, T.-W. Kim, and G.-W. Moon, "Hybrid DC–DC converter using center-tapped clamp circuit in wide range of high output voltage," in *Proc. 10th Int. Conf. Power Electron. ECCE Asia (ICPE-ECCE Asia)*, May 2019, pp. 1921–1926.

[32] C.-Y. Lim, Y. Jeong, M.-S. Lee, K.-H. Yi, and G.-W. Moon, "Half-bridge integrated phase-shifted full-bridge converter with high efficiency using center-tapped clamp circuit for battery charging systems in electric vehicles," *IEEE Trans. Power Electron.*, vol. 35, no. 5, pp. 4934–4945, May 2020, doi: 10.1109/TPEL.2019.2931763.

[33] N. D. Dao, D.-C. Lee, and Q. D. Phan, "High-efficiency SiC-based isolated three-port DC/DC converters for hybrid charging stations," *IEEE Trans. Power Electron.*, vol. 35, no. 10, pp. 10455–10465, Oct. 2020, doi: 10.1109/TPEL.2020.2975124.

[34] P. Sun, L. Zhou, and K. M. Smedley, "A reconfigurable structure DC–DC converter with wide output range and constant peak power," *IEEE Trans. Power Electron.*, vol. 26, no. 10, pp. 2925–2935, Oct. 2011, doi: 10.1109/TPEL.2011.2129576.

[35] M. A. Bakar, F. Alam, M. Das, S. Barg, and K. Bertilsson, "Reconfigurable three state DC–DC power converter for the wide output range applications," in *Proc. 45th Annu. Conf. IEEE Ind. Electron. Soc. (IECON)*, Oct. 2019, pp. 4911–4916, doi: 10.1109/IECON.2019.8927652.

[36] M. A. Bakar and K. Bertilsson, "A modified higher operational duty phase shifted full bridge converter for reduced circulation current," *IEEE Open J. Ind. Electron. Soc.*, vol. 1, pp. 82–96, 2020, doi: 10.1109/OJIES.2020.2994142.

[37] M. A. Bakar, M. F. Alam, M. Wardemark, and K. Bertilsson, "A 2×3 reconfigurable modes wide input wide output range DC–DC power converter," *IEEE Access*, vol. 9, pp. 44292–44303, 2021, doi: 10.1109/ACCESS.2021.3066525.

[38] M. A. Bakar, M. F. Alam, A. Majid, and K. Bertilsson, "Dual-mode stable performance phase-shifted full-bridge converter for wide-input and medium-power applications," *IEEE Trans. Power Electron.*, vol. 36, no. 6, pp. 6375–6388, Jun. 2021, doi: 10.1109/TPEL.2020.3033386.

[39] C.-L. Chen, "Analysis and design for RCD clamped snubber used in output rectifier of phase-shift full-bridge ZVS converters," *IEEE Trans. Ind. Electron.*, vol. 45, no. 2, pp. 358–359, Apr. 1998, doi: 10.1109/41.681236.

[40] *Electric Vehicle Conductive Charging System—Part 23: Dc Electric Vehicle Charging Station*, Standard IEC 61851-23: 2014, European standard, 2014.

[41] H.-M. Fischer. (2013). *Voltage Classes for Electric Mobility*. [Online]. Available: https://www.zvei.org/fileadmin/user_upload/Presse_und_Medien/Publikatio%nen/2014/april/Voltage_Classes_for_Electric_Mobility/Voltage_Classes_for_Elect% ric_Mobility.pdf

[42] U. Badstubner, "Ultra-high performance telecom DC–DC converter," Ph.D. dissertation, Dept. Inf. Technol. Elect. Eng., ETH, Zurich, Switzerland, Apr. 2012. [Online]. Available: https://www.pes-publications.ee.ethz.ch/uploads/tx_ethpublications/UBAd% issOnline.pdf

[43] S. SDI. *SAMSUNG SDI Energy Storage System Technology*. Accessed: Aug. 23, 2021. [Online]. Available: https://www.samsungsdi.com/ess/energy-storage-system-technology.html

[44] J. Muhlethaler, "Modeling and multi-objective optimization of inductive power components," Ph.D. dissertation, Dept. Inf. Technol. Elect. Eng., ETH, Zurich, Switzerland, Jan. 2012. [Online]. Available: https://www.pes-publications.ee.ethz.ch/uploads/tx_ethpublications/Diss% _Muehlethaler.pdf

[45] G. G. Orenchak, "Estimating temperature rise of transformers," Power Electron. Technol., Nashville, Ten, USA, Tech. Rep., Jul. 2004, pp. 14–22.

[46] D. Lyu, T. B. Soeiro, and P. Bauer, "Impacts of different charging strategies on the electric vehicle battery charger circuit using phase-shift full-bridge converter," in *Proc. IEEE 19th Int. Power Electron. Motion Control Conf. (PEMC)*, Apr. 2021, pp. 256–263.

[47] C. Brivio, V. Musolino, M. Merlo, and C. Ballif, "A physically-based electrical model for lithium-ion cells," *IEEE Trans. Energy Convers.*, vol. 34, no. 2, pp. 594–603, Jun. 2019, doi: 10.1109/TEC.2018.2869272.

**Dingsihao Lyu** (Graduate Student Member, IEEE) received the M.Sc. degree in electrical power engineering from the Delft University of Technology, Delft, The Netherlands, in 2019, where he is currently pursuing the Ph.D. degree in electrical engineering with the DC Systems, Energy Conversion, and Storage (DCES) Group.

His research interests include unidirectional/bidirectional dc/dc power electronic converters and multiobjective design of power electronic converters.

**Thiago Batista Soeiro** (Senior Member, IEEE) received the B.Sc. and M.Sc. degrees in electrical engineering from the Federal University of Santa Catarina, Florianópolis (UFSC), Brazil, in 2004 and 2007, respectively, and the Ph.D. degree from the Swiss Federal Institute of Technology, Zürich, Switzerland, in 2012.

From 2012 to 2013, he was a Researcher with the Power Electronics Institute, UFSC. From October 2013 to April 2018, he worked initially as a Scientist and later as a Senior Scientist at the Corporate Research Centre, ABB Switzerland Ltd., Baden-Dattwil, Switzerland. From May 2018 to January 2022, he worked at the DC Systems, Energy Conversion and Storage Group, Delft University of Technology, Delft, The Netherlands. He was a tenured Associate Professor of high power electronics, Delft University of Technology. Since January 2022, he has been with the European Space Agency (ESA), European Space Research and Technology Centre (ESTEC), Noordwijk, The Netherlands, where he works on the research and development of power conditioning and distribution units for aerospace applications.

**Pavol Bauer** (Senior Member, IEEE) received the M.Sc. degree in electrical engineering from the Technical University of Kosice, Košice, Slovakia, in 1985, and the Ph.D. degree from the Delft University of Technology, Delft, The Netherlands, in 1995.

He is currently a Full Professor with the Department of Electrical Sustainable Energy, Delft University of Technology, where he is also the Head of the DC Systems, Energy Conversion and Storage Group. He is also a Professor with the Brno University of Technology, Brno, Czech Republic, and an Honorary Professor with Politehnica University Timişoara, Timişoara, Romania. From 2002 to 2003, he was partially with KEMA, DNVGL, Arnhem, The Netherlands, on different projects related to power electronics applications in power systems. He has worked on many projects for the industry concerning wind and wave energy, power electronic applications for power systems, such as Smarttrafo and HVdc systems, projects for smart cities, such as PV charging of electric vehicles, PV and storage integration, and contactless charging, and participated in several Leonardo da Vinci, H2020, and Electric Mobility Europe EU Projects as a Project Partner (ELINA, INETELE, E-Pragmatic, Micact, Trolley 2.0, OSCD, P2P, and Progressus). He was a Coordinator of PEMCWebLab.com-Edipe, SustEner, and Eranet DCMICRO. He has authored or coauthored more than 120 journal articles and 500 conference papers in his field (with an H-factor of Google Scholar: 40 and Web of Science: 26). He is the author or a coauthor of eight books. He holds seven international patents and organized several tutorials at international conferences. His main research interests include power electronics for charging electric vehicles and dc grids.

Dr. Bauer is the former Chairperson of the Benelux IEEE Joint Industry Applications Society, the Power Electronics and Power Engineering Society Chapter, and the Power Electronics and Motion Control (PEMC) Council, and a member of the Executive Committee of the European Power Electronics Association (EPE) and the international steering committee at numerous conferences.